The Effects of Different Core−Shell Structures on the Electrochemical Performances of Si−Ge Nanorod Arrays as Anodes for Micro-Lithium Ion Batteries

Yingjian Yu,[†] Chuang Yue,[†] Shibo Sun,[†] Wei Lin,[†] Hang Su,[‡] Binbin Xu,[§] Juntao Li,[‡] Suntao Wu,[†] Jing Li,*,[†] and Junyong Kang[†]

[†]Department of Physics/Pen-Tung Sah Institute of Micro-Nano Science and Technology, [‡]School of Energy Research, State Key Lab of Physical Chemistry of Solid Surfaces, College of Chemistry and Chemical Engineering, and [§]College of Chemistry and Chemical Engineering, Xiamen University, Xiamen, Fujian 361005, China

ⓢ *Supporting Information*

ABSTRACT: Connected and airbag isolated Si−Ge nanorod (NR) arrays in different configurations have been fabricated on wafer scale Si substrates as anodes in micro-lithium ion batteries (LIBs), and the impacts of configurations on electrochemical properties of the electrodes were investigated experimentally and theoretically. It is demonstrated that the Si inner cores can be effectively protected by the connected Ge shells and contribute to the enhanced capacity by ∼68%, derived from an activation process along with the amorphization of the crystalline lattice. The first-principles calculations further verify the smaller forces on the Si layers at the atomic level during the restricted volume expansion with the covering of Ge layers. This work provides general guidelines for designing other composites and core−shell configurations in electrodes of micro-LIBs to accomplish higher capacities and longer cycle lives.

KEYWORDS: *lithium ion battery, core−shell structure, silicon−germanium nanorod arrays, capacity proportion, activation, force*
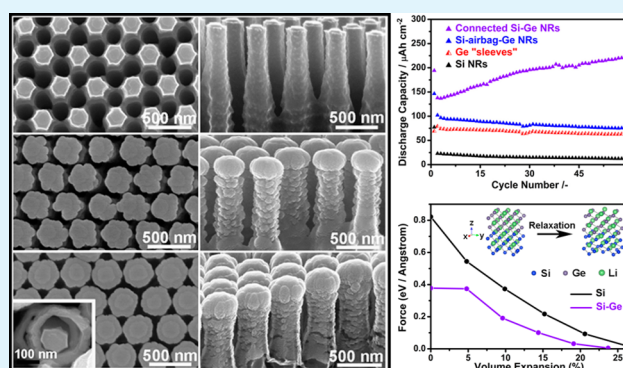
■ INTRODUCTION

Due to the high energy/power density and long working life, rechargeable lithium ion batteries (LIBs) are becoming one of the most promising green energy strategies to resolve the global energy shortage issues.[1−3] Meanwhile, micro/nano-electro-mechanical system (M/NEMS) technologies have developed rapidly so that the demand for appropriately sized micro-LIBs is being driven by the shrinking dimensions of electronic devices.[4,5] It is well accepted that the capacities and performances of micro-LIBs critically depend on the electrode materials and battery configurations. Si, with the highest theoretical capacity of 4200 mAh g^{-1} approximately 10 times higher than that of the currently commercialized graphite (372 mAh g^{-1}), and low working potential by reacting with lithium ion at 0.5 V, has been intensively researched as the electrode material in LIBs and is also a good candidate for fabricating micro-LIBs if considering its feasible integration with other micro- or nano-electronic devices.[6−8] However, the limited practical applications of Si anodes are widely acknowledged due to the capacity fading caused by the large volume expansion (>300%) during cycling.[9,10] In this concern, considerable efforts, such as low dimensional nanostructure synthesis, composite electrode configurations, and so on, have been made to address this volume expansion issue.[11−18] Recently,

kinds of Si-based core−shell nanocomposites, for example, C−Si core−shell nanowires (NWs),[17] double-layered Si−Ge composite nanotube arrays,[18] and so forth, have been investigated as anodes in LIBs presenting excellent electrochemical properties. Generally, in a core−shell structure, the exterior shell can protect the inner core from environmental erosions, inhibit volume expansion, and partake in charge/discharge processes as reversible active materials so that the chemical stability and structure integrity of the electrode can be maintained, resulting in improved battery capacities.[19] However, in most cases, attention is focused on the components of composites and synthesis strategies,[20,21] while the effects of the specific configuration in an individual electrode structure on its electrochemical performances are still less investigated. In other words, some outstanding issues still need to be addressed, for instance: (i) the capacity proportion contributed by the inner cores and outer shells respectively; (ii) can core−shell structures lead to an increment of capacity compared with the sum of the capacities donated by both individual core and shell; (iii) to what extent the outer shells, which themselves

Scheme 1. Illustration of the Fabrication Processes for the Si NR, Connected Si−Ge NR and Si−Airbag−Ge NR Arrays[a]
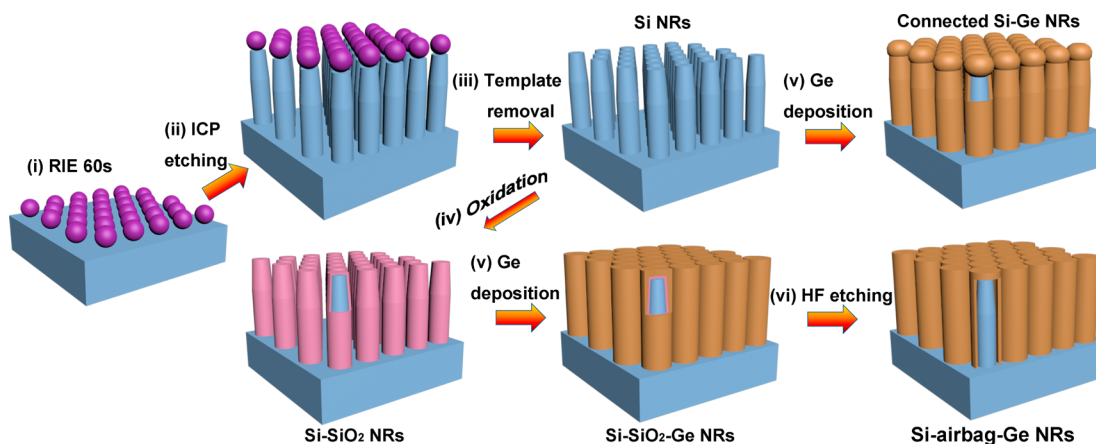
[a](i) Spin-coating of PS nanospheres and O_2 plasma etching on the template, (ii) modified ICP etching with SF_6/C_4F_8 gases to obtain bottlelike Si NR arrays, (iii) template removal by the ultrasonic cleaning, (iv) oxidation of the Si NRs, (v) deposition of an additional Ge film on the Si NRs or Si−SiO_2 NRs using radio frequency (RF) magnetron sputtering with a Ge target, (vi) etching in HF solution.

might be intercalated by lithium ion and bulge during cycling as well, can reduce the volume expansion of inner cores; (iv) how the forces on inner cores would change at an atomic level along with the volume expansion with or without the covering of outer shells.

In this study, Si−Ge core−shell structures in different configurations, so called connected Si−Ge NRs and Si−airbag−Ge NRs, were fabricated as anodes in micro-LIBs on wafer scale Si substrates through a Si-compatible process, including modified nanosphere lithography (NSL), inductive coupled plasma (ICP) dry etching and radio frequency (RF) magnetron sputtering deposition technologies. Configured in periodic array layout and geometrically different Ge compositions, these Si−Ge NR anodes exhibit distinct electrochemical performances, in which the connected Si−Ge nanocomposite electrode presents a much higher capacity than that in the airbag isolated composite anode. First-principles calculations were further performed to investigate the forces in a core−shell structure from an atomic perspective, which evidences the smaller forces on Si layers with the covering of Ge to effectively maintain electrode configuration integrity and thus improve its electrochemical properties. Instead of focusing on synthesis or fabrication of core−shell electrodes with different material compositions and fancy structures, this work experimentally and theoretically investigated the origins of the influences of the core−shell configuration on the corresponding electrochemical properties, which will facilitate the intentional design of core−shell electrodes in micro-LIBs or LIBs to achieve higher capacities and long working lifetimes.

■ EXPERIMENTAL SECTION

Methods. *Preparation of Si−Ge NRs and Si−Airbag−Ge NRs.* As illustrated in Scheme 1, the fabrication for different Si−Ge core−shell structures was performed using a template method based in part on our previous work.[22] Self-assembled polystyrene (PS) nanospheres (5 wt %) with the diameter of 360 nm were spin-coated on n-Si (100) substrates with the thickness of 280−320 μm (Shanghai Guang Wei Electronic Materials Co., Ltd. China) as monodispersive templates followed by an oxygen plasma etching for 60 s to manipulate the size and separation of the templates. Then the inductive coupled plasma (ICP, Alcatel-AMS 200 ICP system) etching was performed on the patterned Si substrates to produce the Si nanorod (NR) arrays. After removal of the PS nanospheres by immersing in tetrahydrofuran,

acetone, and alcohol solutions sequentially with ultrasonic cleaning, piranha solution (4:1 98% H_2SO_4/30% H_2O_2) was used to clean the NR pattered silicon substrates at 80 °C for 10 min. Then the Ge films were deposited on the Si NR arrays by radio frequency (RF) magnetron sputtering (JC-500-3/D) to prepare the Si−Ge NRs using a Ge target with a purity of 99.99%. With regard to the production of Si−airbag−Ge NRs, the Si NRs were firstly oxidized in the O_2 atmosphere at 1000 °C for 30 min to obtain the about 50 nm thick SiO_2 layer, followed by the sputtering deposition of Ge layer at the same run/conditions with above Si−Ge NRs to guarantee the homoousia of the morphologies, active materials' mass and electronic properties, and then immersed in the HF solution. As the Ge outer shell with the thickness of dozens of nm on the side walls was deposited onto the SiO_2 surface by sputtering method, the Ge layer is intrinsically not perfectly dense and must embrace certain degree of porosity. Therefore, when immersing the sample in HF solution for enough time, HF can penetrate through the porous Ge coating to etch away the SiO_2 layer. Also, the regions with imperfect coating of Ge layer would help with the HF solution's diffusion.

Characterization. The morphologies and structure properties of the Si−Ge NRs were investigated using the SU70 thermal field emission scanning electron microscope (SEM), Hitachi S-4800 and LEO1530 field-emission (SEM), and JEM-2100 high resolution transmission electron microscope (HRTEM) equipped with an energy dispersive X-ray (EDX) spectrum analyzer cooperating with Tecnai F30 field emission gun transmission electron microscope (TEM).

For the electrochemical testing, 10×10 mm^2 pieces were cut from the fabricated Si substrates as the anode materials followed by the consecutively sputtering of 20/200 nm Cr/Au on the samples' back side as the current collectors using RF magnetron sputtering at powers of 360/460 W for 90/42 s. Then the connected Si−Ge NRs and Si−airbag−Ge NRs pieces were assembled as the working electrodes in coin cells (2025) with the Si NRs anode as a comparison. In the cells, lithium metal foils were used as the counter electrodes, while a polypropylene (PP) microporous film (Celgard 2400) was chosen as the separator together with the electrolyte of 1 M LiPF$_6$ (lithium hexafluorophosphate) in ethylene carbonate (EC) diethyl carbonate (DEC) (1:1 in volume) and 2% vinylene carbonate (VC). Before electrochemical measurements, the cells were aged for 12 h. The galvanostatic charge and discharge characterization were executed on a Land battery program-control test system within the voltage window from 0.13 to 2.0 V versus Li/Li$^+$ at room temperature.

Theoretical Calculations. The first-principles method based on density functional theory (DFT) was employed to calculate the forces on Si atoms and volume expansions in the Si and Si−Ge composite systems by using the Vienna ab initio simulation package (VASP) code. The projector-augmented waves (PAW) and the local density

approximation (LDA) were used. The 4 × 4 × 1 k-point grids generated by the Monkhorst–Pack scheme were utilized for the structures' relaxation and calculating forces on Si atoms in the 1 × 1 × 5 supercells of the diamond Si and Si–Ge composite structures, respectively, with the plane-wave basis set expanding to a cutoff energy of 400 eV. The Si and Ge slabs were cut in the [100] crystallographic direction and a 16 Å vacuum layer was placed above the Si (100) or Ge (100)/Si(100) unit cells to avoid the interaction between the adjacent cells in the z-axis direction. The Li atoms were inserted into the octahedral and tetrahedral interstices in both the Si and Si–Ge cells.

■ RESULTS AND DISCUSSION

1. The Structures of Si NRs, Si–Ge NRs, Si–Airbag–Ge NRs. As shown in the SEM images of Figure 1, the three kinds
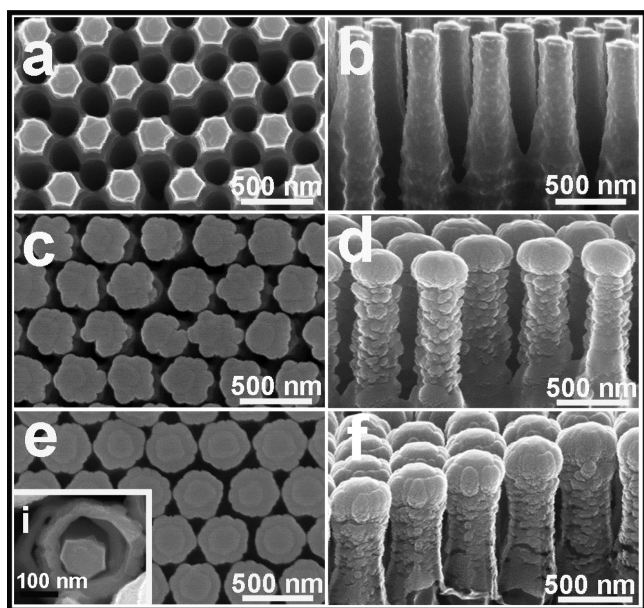

Figure 1. Top-view and section-view SEM images of (a and b) Si NRs, (c and d) connected Si–Ge NRs, and (e and f) Si–airbag–Ge NRs, with a top view of a "cap-taken-off" Si–airbag–Ge NR" in the inset (e,i).

of NRs, Si, Si–Ge, and Si–airbag–Ge NRs are produced in periodic array configuration with different morphologies, and their corresponding images of large areas are shown in Figure S1 (Supporting Information, SI). The Si NRs as seen in Figure 1a and b, in the height of about 3 μm and parallel size of ~240 nm, present the bottlelike hexagonal appearance, the same with our previously reported results.[22] Understandably, with the deposition of Ge film, as in the sample of the connected Si–Ge NR composite, the average size of the NRs increases to ~300 nm while the bottlelike shape is still maintained, as displayed in Figure 1c and d. With regard to the Si–airbag–Ge NRs, in which Si NRs were firstly oxidized forming SiO_2 layer (as shown in Figure S2a-b of SI) followed by Ge film deposition (as displayed in Figure S2c,d of SI) and then etching off the SiO_2, Ge "sleeves" are capping on, but unconnected to, the bottleneck of Si NRs with the total NRs' size enlarged to ~340 nm as seen in Figure 1e and f. The SEM image of an individual "cap-taken-off" Si–airbag–Ge NR as seen in Figure 1e,i was characterized to demonstrate the airbag isolated Si–Ge nanostructure, in which the Ge shell with the thickness of about 30 nm and the specific "airbag" with the space of ~50 nm can be well resolved. By comparing with the morphologies of

$Si–SiO_2–Ge$ NRs, apparently, the Si–airbag–Ge NRs experience the lateral swelling, which is suggested to be caused by the production of the intermediate SiF_4 gas during the etching process.[23,24] The existence of Ge is evidenced by the further electron dispersive spectroscopy (EDS) characterization (Figure S3 of SI). It is worthy to mention that the oxygen element, originally presenting in the configurations of $Si–SiO_2$ NRs and $Si-SiO_2–Ge$ NRs, is dramatically absent in the Si–airbag–Ge NRs within the limit of detection revealing the complete etching of the SiO_2 layers.

More particular morphologies of the Si–Ge NRs and Si–airbag–Ge NRs are detailed in the TEM images of Figure 2. The single Si–Ge NR consists of the monocrystalline Si NR uniformly covered around the body part but densely coated on the top by Ge layer turning out to be a caplike rod as seen in Figure 2a. According to the selective area electron diffraction (SAED) patterns in the insets showing the cloud surrounding the single crystal Si diffraction patterns in the body part and blur circles in the top cap, amorphous-like Ge layer was produced with different thicknesses in the body and top parts of the NR. The boundary between monocrystalline Si and dense amorphous Ge is clearly displayed in Figure 2b, revealing the compact connection between Si and Ge in the connected Si–Ge NR structure. Meanwhile, an intact "Si–airbag–Ge" NR can be visualized in Figure 2c, in which a slenderer Si inner core than that in the connected Si–Ge NR due to the oxidation of Si and then the etching of SiO_2, and the Ge film retained outside the Si NR are presented. A single "sleeve" (Figure 2d,i) peeled off from a Si–airbag–Ge NR and its corresponding elemental mapping patterns as seen in Figure 2d,ii–iv were also characterized, in which only Ge element can be identified. This further evidences the unconnected and loose nature between Ge shell and inner Si NR in the composite nanostructure. Also, the Si(100) plane and thin amorphous Ge layer can be well resolved in the HRTEM image of Figure 2e.

2. The Effects of the Core–Shell Structures on the Electrochemical Performances. In order to demonstrate the effect of the core–shell structures on their electrochemical performances as anodes, capacities with cycling in the electrodes of the connected Si–Ge NRs and Si–airbag–Ge NRs were measured at a current density of 20 μA cm^{-2} within the potential window from 0.13 to 2.0 V versus Li/Li$^+$ by galvanostatic discharge and charge processes, as shown in Figure 3a. Due to the power and energy densities in a small footprint area are the mostly concerned parameters in micro-LIBs,[25−27] the areal capacity (mAh cm^{-2}) is employed to evaluate the ability of Li-ions' insertion/extraction in anodes in this work, which is defined as the total charge/discharge capacity (mAh) divided by the projected surface area (10 mm × 10 mm = 1 cm^2) of the composite electrodes. Si NR anode was also tested as a comparison. Among them, Si NRs as the anode material exhibit the lowest capacity of ~10 μAh cm^{-2} after 60 cycles generally due to the silicon inherent properties such as low electron conductivity and poor lithium ion diffusivity. Undoubtedly, the large volume expansion suffered by Si and formation of solid electrolyte interface (SEI) layer on the surface also deteriorate its electrochemical performances.[28] Compared to Si NRs, Si–airbag–Ge NRs anode presents a higher capacity of ~75 μAh cm^{-2} after 60 cycles resulting from the additional Ge shells acting as the active material, which can partake in the alloying processes with lithium.[29−31] It also can be found that the capacity fades slowly in the first 40 cycles but
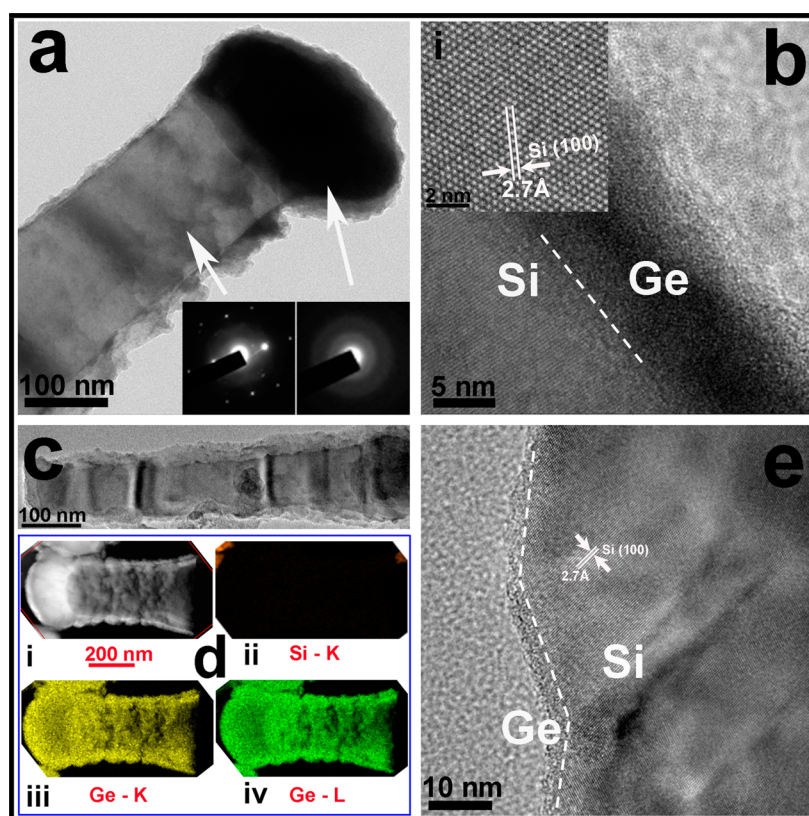
Figure 2. (a) TEM image of a single Si−Ge NR with SAED patterns of cap and body parts of the NR shown in the insets; (b) the corresponding HRTEM image of interface between Si and Ge with the crystalline Si(100) plane lattice displayed in the inset (i); (c) TEM image of an intact Si−airbag−Ge NR; (d) dark-field TEM image of a Ge "sleeve" (i) with corresponding EDX elemental mappings of Si K line (ii), and Ge K and L lines (iii, iv); and (e) HRTEM image of interface between Si and Ge in a Si−airbag−Ge NR.
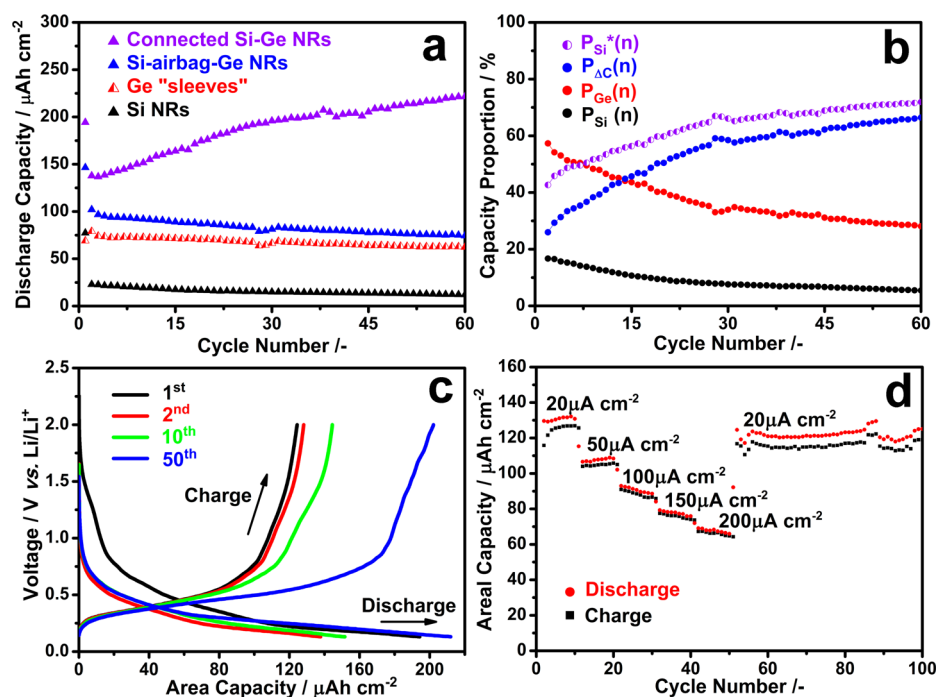
Figure 3. (a) Discharge capacities of Si NRs, Ge "sleeves", Si−airbag−Ge NRs, and connected Si−Ge NRs electrodes under the current of 20 μA cm^{-2} within the voltage window from 0.13 to 2.0 V versus Li/Li$^+$ until 60th cycle. (b) Capacity proportions of the individual Si inner cores, Ge outer shells, increment caused by the specific connected core−shell structure, and the effective capacity of the Si inner cores in the connected Si−Ge NR anode during 1st to 60th cycles. (c) Voltage profiles of the connected Si−Ge NRs electrode for the 1st, 2nd, 10th, and 50th cycles under the current density of 20 μA cm^{-2}. (d) Rate capabilities of the connected Si−Ge NRs electrode at various current densities.

maintains steady after the attenuation, which may be explained by the structure laggardly changing. Minutely, during the initial cycling stage, it is supposed that both the volume expansion and formation of SEI layers on the Si NRs are undergoing since the electrolyte can penetrate through the interstices in the Ge shell and contact directly with the Si surface due to the existence of the airbag and the porosity nature of the Ge shell by sputtering deposition. However, in the next cycles, the Ge "sleeves", which also sustain a volume expansion in the first several lithiation/delithiation processes and finally come into contact with the Si inner core by the Li$^+$ diffusion into the Si through the contact Ge film, would rely on the structural support of Si and help to restrict its bulging. Since all the samples are 10×10 mm^2-sized pieces cut from one Si wafer patterned with periodic hexagonal Si NR arrays and the amount of Ge in every piece is almost the same given the sputtering deposition at one run, capacities of the Si NRs and Si−airbag−Ge NRs can be compared quantitatively. Therefore, the capacity curve of only Ge "sleeves" can be approximately obtained by carrying out the subtraction calculation in corresponding cycles referring to the following equation:

$$C_{Ge}(n) = C_{Si-airbag-Ge\_NRs}(n) - C_{Si\_NRs}(n) \qquad (1)$$

where n is the cycle number from 2 to 60, C_{Ge}, $C_{Si-airbag-Ge\_NRs}$, and C_{Si_NRs} stand for the capacities of Ge "sleeves", Si−airbag−Ge NRs, and Si NRs electrodes in the corresponding cycle, respectively. As a result, the Ge "sleeves" retain the capacity of not less than 60 μAh cm^{-2} even after 60 cycles due to not only its relatively higher electron conductivity and lithium ion diffusivity but also the loose structure, which would facilitate the lithium ion insertion/extraction processes.

On the other hand, the connected Si−Ge NR anode exhibits the absolutely highest capacity of ~220 μAh cm^{-2} with an apparent capacity rising process until 60 cycles, which is suggested to be caused by the enhanced Li-ion diffusion kinetics in a composite structure during the activation and stabilization cycles.[32,33] Due to the protection of Ge outer shell around the Si NRs, the formation of SEI layer is avoided on the majority of Si surface, which is favorable for lithium ions' layer-by-layer diffusion into the Si material, resulting in a sufficient activation process.[22,34,35] Meanwhile, as the volume expansion of Ge (>270%) during cycling is smaller than that in Si anodes (>300%),[9,36] the swelling of Si NRs can be restricted by the connected outer layer of Ge. In addition, the alloy of the Ge film with the lithium will also contribute to the overall capacity. Therefore, the highest capacity is understandably embraced by the connected Si−Ge NR anode for micro-LIBs compared with either only Si NR or Si−airbag−Ge NR electrodes. Interestingly, but not unexpectedly, the capacity of the connected Si−Ge NRs electrode is much higher than the sum of the capacities donated by individual Si inner cores and Ge outer shell sleeves calculated above. To comprehend the constitutions of the capacity, the proportion contributed by individual Si inner cores ($P_{Si}(n)$) and Ge outer shells ($P_{Ge}(n)$) during the cycling are given by

$$P_{Si}(n) = C_{Si\_NRs}(n)/C_{Si-Ge\_NRs}(n) \times 100\% \qquad (2)$$

$$P_{Ge}(n) = C_{Ge}(n)/C_{Si-Ge\_NRs}(n) \times 100\% \qquad (3)$$

The increment ($\Delta C(n)$) caused by the specific core−shell structure and its proportion ($P_{\Delta C}(n)$) are given by

$$\Delta C(n) = C_{Si-Ge\_NRs}(n) - C_{Si-airbag-Ge\_NRs}(n) \qquad (4)$$

$$P_{\Delta C}(n) = \Delta C(n)/C_{Si-Ge\_NRs}(n) \times 100\% \qquad (5)$$

Figure 3b reveals the declining trends of $P_{Si}(n)$ and $P_{Ge}(n)$ after continuous cycling; however, $P_{\Delta C}(n)$ increases notably up to ~62%, revealing the positive effect of the connected core−shell structure on the capacity of Si−Ge NRs anode. This effect can be attributed to the closely contact Si−Ge composite configuration that hinders the growth of an SEI layer on the inner cores by preventing direct contact between the active Si material and the electrolyte. This protective behavior improves the electrochemical kinetics by utilizing the outer shells of the Ge and restraining the volume expansion to avoid the mechanical breakage. These effects were also invoked by Wang et al. for a different phenomenon.[37] Because the surface environment of the Si inner cores is the most obvious difference between the connected Si−Ge NRs and the Si−airbag−Ge NRs, $\Delta C(n)$ should be mostly burdened by the Si inner cores. Accordingly, the effective capacity of the Si inner cores ($C_{Si\_NRs}*(n)$) in the connected Si−Ge NRs anode as well as its contributed proportion ($P_{Si}*(n)$) is given by

$$C_{Si\_NRs}*(n) = C_{Si\_NRs}(n) + \Delta C(n) \qquad (6)$$

$$P_{Si}*(n) = C_{Si\_NRs}*(n)/C_{Si-Ge\_NRs}(n) \times 100\% \qquad (7)$$

$$P_{Si}*(n) = P_{Si}(n) + P_{\Delta C}(n) \qquad (8)$$

Consequently, the core−shell structure retains and stimulates the activity of the inner Si cores during the cycling, as indicated by the increasing $P_{Si}*(n)$ up to ~68%, as shown in Figure 3b.

The connected Si−Ge NRs electrode manifests the first discharge capacity of ~195 μAh cm^{-2} and the first charge capacity of ~125 μAh cm^{-2} with an restricted initial Coulombic efficiency (CE) of 64.1% in the voltage window from 0.13 to 2.0 V versus Li/Li$^+$ (Figure 3c), which is still much higher than 30.0% of only Si NRs anode (SI, Figure S4) and comparable to our previous work.[22,38] After the first cycle, the decelerating or ceasing of the side reactions is responsible for the improving CE of the Si−Ge electrode, 93.0% in the 2nd, 95.2% in the 10th, and 95.4% in the 50th cycle. Although, due to the volume expansion in both Si and Ge and solid electrolyte interface (SEI) layers' formation on the electrode surface, the CE is not very satisfied; it is still comparable to previous Si−Ge based electrode materials.[39] Of course, further optimizing the fabrication process, such as interface alternation, structure modification, and so on, may help to improve the performances. During the first Li-ion insertion process, the alloying reaction of the Ge outer shells with lithium is evidenced by the first voltage plateau located between 0.25 and 0.5 V, followed by the alloying reactions of both Si and Ge with lithium indicated by the downward slope plateau under 0.25 V.[18] Meanwhile, the activation effect is also presented during the whole 1st to 50th cycles, resulting in the improved total charge capacity. Furthermore, the decaying in discharge capacity of the connected core−shell structured Si−Ge NRs electrode can be found in Figure 3d, from ~130 μAh cm^{-2} at the current density of 20 μA cm^{-2} to ~66 μAh cm^{-2} at that of 200 μA cm^{-2}; even so, the electrode resumes an ~120 μAh cm^{-2} capacity lasting until the 100th cycle when the current density is reduced to 20 μA cm^{-2} again. Significantly, there is a slight activation process in the first 20 cycles under the current densities of 20 and 50 μA cm^{-2}, after which the activation process disappears in despite of the restoring of the 20 μA cm^{-2} current density. Therefore, a low current density is essential to achieve the

activation purpose since the inconvertible structure breaches caused by the high current densities would occur even with the restriction of the Ge outer shells.

The post morphologies of the connected Si−Ge NR and Si−airbag−Ge NR composite anodes after 100 cycles were characterized by SEM and TEM as seen in SI Figure S5. Due to the participation of both the inner Si NRs and Ge outer shells in the lithiation/delithiation process, the connected Si−Ge NRs undergo some volume expansion with cycling but still well maintaining its original layout, as shown in SI Figure S5a−c. In comparison, the Si NR arrays with very little Ge coating were presented in the cycled Si−airbag−Ge NR electrode due to the peeling of the Ge shells possibly during the repeated discharging/charging processes and the later sample preparation procedure, as shown in SI Figure S5d−f, also indicating the loose contact between the Si inner cores and Ge shells. What's more, the barely changing of the Si NRs in the morphology as seen in SI Figure S5d further evidences that only small portion of Si alloyed with lithium as discussed above.

3. The Lithiation Process in the Specific Core−Shell Structured Si−Ge Composite. Furthermore, the ab initio first-principles method is often employed to investigate lithium ion diffusion in Si or Si−Ge system in recent years,[18,34] which was also utilized to understand the lithiation process in the Si−Ge core−shell composites from an atomic perspective, as illustrated in Figure 4. Compared to the 26.3% volume
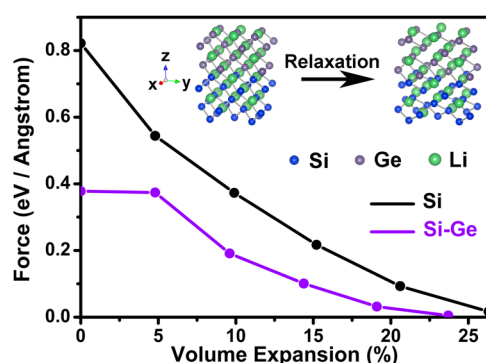
Figure 4. DFT calculations for the average force on the Si atoms within the Si and Si−Ge composite systems during volume expansion.

expansion in a pure Si unit cell with full Li atom occupation of the octahedral and tetrahedral interstices, the portion of the Si lattice in the Si−Ge composite system experiences a smaller growth (23.7%). Additionally, the average magnitude of the forces on the Si atoms along the z-axis in the Si−Ge system is smaller than that in the Si-only unit cell during the entire relaxation process, revealing the contribution of Ge toward relieving the pressure on the Si atoms during swelling. Of course, the intrinsically smaller volume expansion in the Ge lattice induced by the lithiation process would restrain the expansion of Si lattice via the counterforce.[18] As a result, the core−shell configuration can be well maintained and thus the corresponding electrochemical performances would be effectively manipulated.

CONCLUSIONS

In conclusion, connected Si−Ge composite anodes were fabricated for comparison with airbag isolated structures to demonstrate the specific effects of the core−shell structure on improved electrochemical performances. On one hand, Ge

shells protect the Si inner NRs from the electrolyte to hinder the formation of SEI layers, so that the activation processes along with the amorphization of crystalline Si can enhance the capacity. On the other hand, the restricted volume expansion and smaller forces on the inner Si cores due to the covering of the Ge outer shells were verified experimentally and theoretically, which helps to stabilize the configuration of the core−shell NR array electrodes. Further experimental optimization is hopeful to sufficiently utilize the positive effect of the core−shell nanostructure in electrodes for better electrochemical performances in micro-LIBs or LIBs. In addition to the Si−Ge series nanorods, the procedures and demonstrations in this work also provide experiences for designing other composites, such as Si−Sn system, and core−shell configurations, such as spheres, in electrode materials for micro-LIBs or LIBs, to obtain higher capacities and longer working lifetime.

ASSOCIATED CONTENT

Ⓢ Supporting Information
Additional figures of the morphology and electrochemical characterization. This material is available free of charge via the Internet at http://pubs.acs.org.

AUTHOR INFORMATION

Corresponding Author
*E-mail: lijing@xmu.edu.cn (J. L.).

Notes
The authors declare no competing financial interest.

ACKNOWLEDGMENTS

REFERENCES

(1) Tarascon, J.-M.; Armand, M. Issues and Challenges Facing Rechargeable Lithium Batteries. *Nature* **2001**, *414*, 359−367.
(2) Armand, M.; Tarascon, J.-M. Building Better Batteries. *Nature* **2008**, *451*, 652−657.
(3) Duun, B.; Kamath, H.; Tarascon, J.-M. Electrical Energy Storage for the Grid: A Battery of Choices. *Science* **2011**, *334*, 928−935.
(4) Roberts, M.; Johns, P.; Owen, J.; Brandell, D.; Edstrom, K.; Enany, G. E.; Guery, C.; Golodnitsky, D.; Lacey, M.; Lecoeur, C.; Mazor, H.; Peled, E.; Perre, E.; Shaijumon, M. M.; Simon, P.; Taberna, P.-L. 3D Lithium Ion Batteries - from Fundamentals to Fabrication. *J. Mater. Chem.* **2011**, *21*, 9876−9890.
(5) Song, J.; Yang, X.; Zeng, S.-S.; Cai, M.-Z.; Zhang, L.-T.; Dong, Q.-F.; Zheng, M.-S.; Wu, S.-T.; Wu, Q.-H. Solid-State Microscale Lithium Batteries Prepared with Microfabrication Processes. *J. Micromech. Microeng.* **2009**, *19*, 045004.
(6) Boukamp, B. A.; Lesh, G. C.; Huggins, R. A. All-Solid Lithium Electrodes with Mixed-Conductor Matrix. *J. Electrochem. Soc.* **1981**, *128*, 725−729.
(7) Sharma, R.A.; Seefurth, R. N. Thermodynamic Properties of the Lithium-Silicon System. *J. Electrochem. Soc.* **1976**, *123*, 1763−1768.
(8) Lai, S.-C. Solid Lithium-Silicon Electrode. *J. Electrochem. Soc.* **1976**, *123*, 1196−1197.
(9) Kasavajjula, U.; Wang, C. S.; Appleby, A. J. Nano- and Bulk-Silicon-Based Insertion Anodes for Lithium-Ion Secondary Cells. *J. Power Sources* **2007**, *163*, 1003−1039.

(10) Zhao, K.; Wang, W. L.; Gregoire, J.; Pharr, M.; Suo, Z.; Vlassak, J. J.; Kaxiras, E. Lithium-Assisted Plastic Deformation of Silicon Electrodes in Lithium-Ion Batteries: A First-Principles Theoretical Study. *Nano Lett.* **2011**, *11*, 2962−2967.

(11) Park, M.-H.; Kim, M. G.; Joo, J.; Kim, K.; Kim, J.; Ahn, S.; Cui, Y.; Cho, J. Silicon Nanotube Battery Anodes. *Nano Lett.* **2009**, *9*, 3844−3847.

(12) Chan, C. K.; Patel, R. N.; O'Connell, M. J.; Korgel, B. A.; Cui, Y. Solution-Grown Silicon Nanowires for Lithium-Ion Battery Anodes. *ACS Nano* **2010**, *4*, 1443−1450.

(13) Xia, F.; Kim, S. B.; Cheng, H.; Lee, J. M.; Song, T.; Huang, Y.; Rogers, J. A.; Paik, U.; Park, W. I. Facile Synthesis of Free-Standing Silicon Membranes with Three-Dimensional Nanoarchitecture for Anodes. *Nano Lett.* **2013**, *13*, 3340−3346.

(14) Ruffo, R.; Hong, S. S.; Chan, C. K.; Huggins, R. A.; Cui, Y. Impedance Analysis of Silicon Nanowire Lithium Ion Battery Anodes. *J. Phys. Chem. C* **2009**, *113*, 11390−11398.

(15) Wu, H.; Chan, G.; Choi, J. W.; Ryu, I.; Yao, Y.; McDowell, M. T.; Lee, S. W.; Jackson, A.; Yang, Y.; Hu, L. B.; Cui, Y. Stable Cycling of Double-Walled Silicon Nanotube Battery Anodes Through Solid-Electrolyte Interphase Control. *Nat. Nanotechnol.* **2012**, *7*, 310−315.

(16) Liu, N.; Wu, H.; McDowell, M. T.; Yao, Y.; Wang, C.; Cui, Y. A Yolk-Shell Design for Stabilized and Scalable Li-Ion Battery Alloy Anodes. *Nano Lett.* **2012**, *12*, 3315−3321.

(17) Cui, L.-F.; Yang, Y.; Hsu, C.-M.; Cui, Y. Carbon-Silicon Core-Shell Nanowires as High Capacity Electrode for Lithium Ion Batteries. *Nano Lett.* **2009**, *9*, 3370−3374.

(18) Song, T.; Cheng, H.; Choi, H.; Lee, J.-H.; Han, H.; Lee, D. H.; Yoo, D. S.; Kwon, M.-S.; Choi, J.-M.; Doo, S. G.; Chang, H.; Xiao, J.; Huang, Y.; Park, W. I.; Chuang, Y.-C.; Kim, H.; Rogers, J. A.; Paik, U. Si/Ge Double-Layered Nanotube Array as a Lithium Ion Battery Anode. *ACS Nano* **2012**, *6*, 303−309.

(19) Su, L.; Jing, Y.; Zhou, Z. Li Ion Battery Materials with Core-Shell Nanostructure. *Nanoscale* **2011**, *3*, 3967−3983.

(20) Ng, S.-H.; Wang, J.; Wexler, D.; Konstantinov, K.; Guo, Z.-P.; Liu, H.-K. Highly Reversible Lithium Storage in Spheroidal Carbon-Coated Silicon Nanocomposites as Anodes for Lithium-Ion Batteries. *Angew. Chem., Int. Ed.* **2006**, *45*, 6896−6899.

(21) Cao, F.-F.; Deng, J.-W.; Xin, S.; Ji, H.-X.; Schmidt, O. G.; Wan, L.-J.; Guo, Y.-G. Cu-Si Nanocable Arrays as High-Rate Anode Materials for Lithium-Ion Batteries. *Adv. Mater.* **2011**, *23*, 4415−4420.

(22) Yue, C.; Yu, Y.; Yin, J.; Wong, T.; Zang, Y.; Li, J.; Kang, J. Fabrication of 3D Hexagonal Bottle-like Si-SnO₂ Core-Shell Nanorod Arrays as Anode Materials in on Chip Micro-Lithium-Ion-Batteries. *J. Mater. Chem. A* **2013**, *1*, 7896−7904.

(23) Judge, J. S. A Study of the Dissolution of SiO₂ in Acidic Fluoride Solutions. *J. Electrochem. Soc.* **1971**, *118*, 1772−1775.

(24) Mikeska, R.; Bennison, J.; Grise, S. L. Corrosion of Ceramics in Aqueous Hydrofluoric Acid. *J. Am. Ceram. Soc.* **2000**, *83*, 1160−1164.

(25) Dunn, B.; Kim, C.-J.; Tolbert, S. Three-Dimensional Micro-batteries for MEMS/NEMS technology. *IEEE Int. Conf. Micro Electro Mech. Syst., 23rd* **2010**, 164−167.

(26) Cheah, S. K.; Perre, E.; Rooth, M.; Fondell, M.; Harsta, A.; Nyholm, L.; Boman, M.; Gustafsson, T.; Lu, L.; Simon, P.; Edstrom, K. Self-Supported Three-Dimensional Nanoelectrodes for Microbattery Applications. *Nano Lett.* **2009**, *9*, 3230−3233.

(27) Baggetto, L.; Knoops, H. C. M.; Niessen, R. A. H.; Kessels, W. M. M.; Notten, P. H. L. 3D Negative Electrode Stacks for Integrated All-Solid-State Lithium-Ion-Microbatteries. *J. Mater. Chem.* **2010**, *20*, 3703−3708.

(28) Wachtler, M.; Besenhard, J. O.; Winter, M. Tin and Tin-Based Intermetallics as New Anode Materials for Lithium-Ion Cells. *J. Power Sources* **2001**, *94*, 189−193.

(29) Yoon, S.; Park, C.-M.; Sohn, H.-J. Electrochemical Character-izations of Germanium and Carbon-Coated Germanium Composite Anode for Lithium Ion Batteries. *Electrochem. Solid-State Lett.* **2008**, *11*, A42−A45.

(30) Graetz, J.; Ahn, C. C.; Yazami, R.; Fultz, B. Nanocrystalline and Thin Film Germanium Electrodes with High Lithium Capacity and High Rate Capabilities. *J. Electrochem. Soc.* **2004**, *151*, A698−A702.

(31) Kennedy, T.; Mullane, E.; Geaney, H.; Osiak, M.; O'Dwyer, C.; Ryan, K. M. High-Performance Germanium Nanowire-Based Lithium-Ion Battery Anodes Extending over 1000 Cycles Through in Situ Formation of a Continuous Porous Network. *Nano Lett.* **2014**, *14*, 716−723.

(32) Zeng, L.; Xiao, F.; Wang, J.; Gao, S.; Ding, X.; Wei, M. ZnV₂O₄-CMK Nanocomposite as an Anode Material for Rechargeable Lithium-Ion Batteries. *J. Mater. Chem.* **2012**, *22*, 14284−14288.

(33) Shi, Y. F.; Guo, B. K.; Corr, S. A.; Shi, Q. H.; Heier, Y. S.; Hu, K. R.; Chen, L. Q.; Seshadri, R.; Stucky, G. D. Ordered Mesoporous Metallic MoO₂ Materials with Highly Reversible Lithium Storage Capacity. *Nano Lett.* **2009**, *9*, 4215−4220.

(34) Zhang, Q.; Zhang, W.; Wan, W.; Cui, Y.; Wang, E. Lithium Insertion on Silicon Nanowires: an ab initio Study. *Nano Lett.* **2010**, *10*, 3243−3249.

(35) Liu, X. H.; Wang, J. W.; Huang, S.; Fan, F.; Huang, X.; Liu, Y.; Krylyuk, S.; Yoo, J.; Dayeh, S. A.; Davydov, A. V.; Mao, S. X.; Picraux, S. T.; Zhang, S.; Li, J.; Zhu, T.; Huang, J. Y. In situ Atomic-Scale Imaging of Electrochemical Lithiation in Silicon. *Nat. Nanotechnol.* **2012**, *7*, 749−756.

(36) Alcantara, R.; Tillard-Charbonnel, M.; Spina, L.; Belin, C.; Tirado, J. L. Electrochemical Reactions of Lithium with Li₂ZnGe and Li₂ZnSi. *Electrochim. Acta* **2002**, *47*, 1115−1120.

(37) Wang, B.; Li, X.; Zhang, X.; Luo, B.; Zhang, Y.; Zhi, L. Contact-Engineered and Void-Involved Silicon/Carbon Nanohybrides as Lithium-Ion-Battery Anodes. *Adv. Mater.* **2013**, *25*, 3560−3565.

(38) Li, J.; Yue, C.; Yu, Y.; Chui, Y.-S.; Yin, J.; Wu, Z.; Wang, C.; Zang, Y.; Lin, W.; Li, J.; Wu, S.; Wu, Q. Si/Ge Core-Shell Nanoarrays as the Anode Material for 3D Lithium Ion Batteries. *J. Mater. Chem. A* **2013**, *1*, 14344−14349.

(39) Song, T.; Cheng, H.; Town, K.; Park, H.; Black, R. W.; Lee, S.; Park, W. I.; Huang, Y.; Rogers, J. A.; Nazar, L. F.; Paik, U. Electrochemical Properties of Si-Ge Heterostructures as an Anode Material for Lithium Ion Batteries. *Adv. Funct. Mater.* **2014**, *24*, 1458−1464.